Published in final edited form as:
Magn Reson Med. 2010 December ; 64(6): 1625–1639. doi:10.1002/mrm.22552.

Performance of external and internal coil configurations for prostate investigations at 7 Tesla

Gregory J. Metzger[1], **Pierre-Francois van de Moortele**[1], **Can Akgun**[1], **Carl J. Snyder**[1], **Steen Moeller**[1], **John Strupp**[1], **Peter Andersen**[1], **Devashish Shrivastava**[1], **Tommy Vaughan**[1], **Kamil Ugurbil**[1], and **Gregor Adriany**[1]

[1]University of Minnesota Medical School, Center for Magnetic Resonance Research, Minneapolis, Minnesota 55455, USA

Abstract

Three different coil configurations were evaluated through simulation and experimentally to determine safe operating limits and evaluate subject size dependent performance for prostate imaging at 7 Tesla. The coils included a transceiver endorectal coil (trERC), a 16 channel transceiver external surface array (trESA) and a trESA combined with a receive-only ERC (trESA +roERC). While the transmit B_1 (B_1^+) homogeneity was far superior for the trESA, the maximum achievable B_1^+ is subject size dependent and limited by transmit chain losses and amplifier performance. For the trERC, limitations in transmit homogeneity greatly compromised image quality and limited coverage of the prostate. Despite these challenges, the high peak B_1^+ close to the trERC and subject size independent performance provides potential advantages especially for spectroscopic localization where high bandwidth RF pulses are required. On the receive side, the combined trESA+roERC provided the highest SNR and improved homogeneity over the trERC resulting in better visualization of the prostate and surrounding anatomy. In addition, the parallel imaging performance of the trESA+roERC holds strong promise for diffusion weighted imaging and dynamic contrast enhanced MRI.

Keywords

Prostate; 7 Tesla; Endorectal Coil; Stripline Array; Body Imaging

INTRODUCTION

Anatomic and functional magnetic resonance imaging (MRI) has been shown to be a valuable tool in staging prostate cancer above and beyond what is possible with standard clinical tests such as digital rectal exams, transrectal ultrasound guided biopsy and serum prostate specific antigen (PSA) measures (1). While anatomic MRI based primarily on T2-weighted contrast provides delineation of zonal anatomy, extracapsular extension, and regions of cancer, functional MRI studies have been shown to further increase sensitivity and specificity over anatomic imaging alone by improving the differentiation of cancer from benign processes. Many studies have demonstrated the utility of combining anatomic imaging with various combinations of functional studies in determining disease volume, targeting biopsy, treatment planning and therapy monitoring (2-5).

Send Correspondence to: Greg Metzger, Ph.D. Center for Magnetic Resonance Research University of Minnesota 2021 6th Street S.E. Minneapolis, MN 55455 gmetzger@umn.edu Phone: 612-626-2001 Fax: 612-626-2004.

As with many other applications, the impetus behind the use of higher magnetic field for prostate MRI is driven by the promise of improved disease characterization resulting from increased spectral dispersion, parallel imaging performance, and signal-to-noise ratio (SNR). When comparing 3T with 1.5T, increase in SNR alone has resulted in a diagnostically relevant increase in spatial resolution which is crucial for the identification of extracapsular extension in anatomic T2-weighted images, and for decreasing partial voluming in spectroscopy studies thus improving the identification and characterization of smaller volumes of disease (6,7). Increasing field strength also results in increased spectral resolution in spectroscopy, increasing the potential to quantify individual metabolites (8) and to lead to more sensitive and specific biomarkers as demonstrated in high resolution magic angle spinning spectroscopy (HRMAS) spectra of prostate cancer tissue (9).

Increased temporal resolution directly benefits dynamic contrast enhanced MRI (DCE-MRI) where higher temporal sampling has been shown to improve the determination of pharmacokinetic parameters used to characterize neovascularization (10). In addition to increasing SNR and thus spatial resolution, the increase in field strength can be used to improve temporal resolution by reducing the necessity to signal average and, even more significantly, by improved parallel imaging performance. It was shown by Wiesinger et al. (11) that the increased spatial encoding capability of the receive B_1 field (B_1^-) of each coil element at high field can be used to increase reduction factors (R) while maintaining a relatively low geometry factor (g-factor). Maintaining a low g-factor is critical as it inversely scales the resulting SNR for a given R based on the relation $\mathrm{SNR} \propto 1/(g*\sqrt{R})$.

In order to take full advantage of the promise of prostate MRI, coil configurations have been optimized based of different design criteria. Initially, to improve the SNR of prostate studies at 1.5T, receive only external surface arrays (roESA) were combined with receive only endorectal coils (roERC). However, with the arrival of the clinical 3T platform, some studies returned to focus on the roESA alone where the field strength dependent increase in SNR provided a similar performance compared to the combined roERC+roESA coil at 1.5T (12). While there are several advantages to the sole use of an roESA, the diagnostic information obtained with the roERC (13) and roESA+roERC coils (6) at 3T have been demonstrated to be superior.

Optimizing RF coil configurations for ultra high field (UHF) applications, i.e. higher than 3T, requires attention to additional issues not present on lower field systems. For example, UHF whole body MRI systems typically do not make use of whole body RF transmit coils due to the increased power requirements and power deposition in tissues, both roughly proportional to B_0^2 (14). In the absence of a whole body volume transmit coil, local transmit coils must be developed and typically each of these transmit coil elements are also utilized as receive coil elements (then referred to as transceiver coil elements).

Beyond roESA and roERC coils currently in use clinically, there are several examples where local transmit coils have been developed for prostate imaging. Transceiver external surface arrays (trESA) have been previously presented for use at field strengths of 3T (15,16), 4T (17) and 7T (18). Other coil configurations have included a trESA in combination with a roERC at 4T (19) and transceiver ERCs (trERC) at 7T (20-22). Each of these coil configurations has advantages and disadvantages. The trERC coils developed for 7T prostate imaging provide the advantage of high SNR and high peak transmit B_1 (B_1^+) but suffer greatly from receive B_1 (B_1^-) and B_1^+ inhomogeneity. The trESA coils, even at lower field strengths, provide the ability for B_1^+ shimming (or field focusing) resulting in increased transmit efficiency compared to whole body volume transmit. While the trESA coils can provide homogeneous transmit and receive profiles in the prostate, they cannot achieve the maximum SNR and peak $B_1^+$of the local trERC. Finally, the combination of a trESA with a

roERC provides the flexibility of B_1^+ shimming while maintaining the SNR advantages of the ERC but still lacks the peak B_1^+ of a trERC coil.

While the previously described coil configurations are all options for prostate imaging at 7T, the challenges of optimizing these coils in terms of performance and safety greatly increase with field strength. These challenges are a result of the quadratic relationship between B_0 and RF power as well as the increasingly complex B_1^+ fields. With respect to performance, it was sufficient at 3T and 4T to predetermine B_1^+ shimming solutions determined from the geometric design of trESA RF coils (15-17). However, this one size fits all approach becomes far less optimal at 7 T, where the RF wavelength becomes as short as ~12 cm in the body, so that B_1^+ fields vary much more rapidly and are increasingly affected by body geometry and coil position. This has been experimentally demonstrated in the work done at 7T using a trESA coil, where a subject dependent B_1^+ shimming method (rather than a unique, coil based method) was employed (18). With respect to safety, the *E*-fields are responsible for RF induced heating in the body and, at 7T, they surpass the B_1^+ fields in term of spatial complexity. An important consequence of the latter is that at UHF the most constraining limits on RF power, with regards to patient safety, are typically the result of local rather than whole body heating. These local effects become even more prominent when using transmit coils that are positioned close to, as well as inside, the body as in the present study. Understanding these local *E*-fields and/or local heating is of paramount importance for determining safe operating limits while not unnecessarily limiting power which would compromise performance.

In this paper, we developed three different coil configurations at 7T and investigated their characteristics: a transceiver ERC coil (trERC), a transceiver external surface array (trESA) and a trESA combined with a receive only ERC (roERC) which will be referred to as a trESA+roERC. These coils were evaluated by simulation, phantom studies and in vivo studies to determine parallel imaging performance, SNR and receive B_1 (B_1^-) homogeneity, transmit B_1 (B_1^+) homogeneity and peak B_1^+ performance under the constraints of available RF power and local specific absorption rates (SAR) or heating limits.

METHODS

Magnet and RF subsystems

Phantom and *in vivo* data were acquired on a Magnex (Magnex, Oxford, UK) 7T, 90cm bore magnet with a Siemens 32 channel console, using whole body gradients and 16 RF transceiver channels. For this setup, the RF transmit path of each coil element was equipped with a broadband T/R switch and preamplifier (Varian Inc, Palo Alto, CA). For RF transmission, 16 × 1 kW amplifiers (CPC, Hauppauge, NY) were used when transmitting with the trESA either by itself or in combination with the roERC (23,24). The phase and gain of the low voltage input of the 16 amplifiers were modulated by a remotely controlled multi channel RF phase and gain unit (CPC, Hauppauge, NY). When using the trERC, a single 1 kW RF amplifier was used for RF transmission. In all cases, power optimization was determined in the region of the prostate based on calculated B_1^+ maps acquired using the double flip angle method (DAM) (25).

In addition to the standard MR console RF power monitoring system of forward and reflected power for one channel, a similar 16-channel RF power monitoring system was developed in-house. The RF power amplifiers for each of the 16 RF channels were equipped with a directional coupler that provides an attenuated version of the output waveform. In order to estimate the instantaneous power, a diode based envelope detector circuit was used to rectify and smooth the forward power signal to a quasi-static signal to allow for ADC sampling at a moderate rate of 50 kHz. Each channel of the system was calibrated by

measuring the peak-to-peak voltage delivered to a 50 Ω terminator at the position of the coil. This RF voltage measurement was used to calculate the power delivered to the coil with respect to the plateau voltage of the pulse envelope measured with the diode detector.

The system maintains additionally a 10 second and 5 minute moving average. If the mean power over the 5 minute window exceeds the coil dependent time average power limit (TAP_{limit}) on any transmit channel, all RF amplifiers are immediately disabled until manually reset by the operator. The determination of TAP_{limit} for the trESA and trERC are described below. The monitoring software is written in LabVIEW and runs on a controller board housed in a PXI chassis along with the ADC boards (National Instruments Corporation, Austin, TX). A remote host GUI is provided to the operator for setting the threshold limits and allows for viewing graphically the current average RF doses on a per channel basis.

Local B_1^+ phase shimming

Local B_1^+ phase shimming was performed in all simulations and experiments in which multiple transmit channels were used. Experimentally, local B_1^+ phase shimming used methods previously published by our group (18). Briefly, a series of low-resolution, low flip angle GRE images were acquired while pulsing RF power through only one channel at a time. This was accomplished for all 16 transmit channels in a single acquisition by setting up a dynamic table used by the CPC's phase and gain controller. The relative transmit B_1^+ phases were then calculated for each channel and used to perform local B_1^+ phase shimming. B_1^+ shimming consisted of drawing a region of interest around the prostate in which, for each channel the average relative transmit phase was determined and subtracted through the remotely controlled multi channel RF phase and gain unit. For the region within the chosen ROI, the procedure maximizes the transmit efficiency. For the 16 channel ESA used in this work, local B_1^+ shimming required approximately 2 minutes to acquire the subject dependent calibration data as well as calculate and apply the optimal phases.

Coil Design

A 16 channel external surface array (ESA) similar to that previously described and characterized consisted of two 8-element TEM stripline arrays, positioned anterior and posterior to the pelvis (26,27). Figure 1a shows the coil positioned on a volunteer with >1 cm padding between the coil and patient. The eight coil elements within each of the two arrays were attached in parallel configuration with minimal gap between two polytetrafluoroethylene (PTFE) plates measuring 22.7×35.6 cm^2 with 0.3 cm thickness flexed to have a fixed curvature of 4 degrees. The anterior array, without the patient side PTFE plate, is shown in Fig. 1b. The individual coil elements were 15.3 cm long with a 1.27 cm wide inner conductor and a 5.0 cm wide outer conductor, separated by a 1.9 cm thick PTFE dielectric bar stock with a low loss tangent and a permittivity of 2.08. All elements were individually tuned to 297 MHz (7T), and matched to a 50Ω coaxial line. Capacitive decoupling facilitated more than 21 dB isolation between elements when unloaded and 26 dB isolation when loaded. Figure 1c shows a diagram depicting the relative positioning of the tuning, matching and decoupling capacitors all of which are variable in the range of 1 to 10 pF.

The transmit-receive endorectal loop coil (trERC) was built from a modified commercially available inflatable 3T endorectal coil (Medrad, Pittsburgh, PA) where the conductor and circuitry were completely replaced. The basic housing of this coil includes a 32 cm flexible plastic rod with a balloon surrounding the distal 7 cm. The rod extends through the middle of the balloon providing rigidity for coil insertion and houses both the conductor leading up to the tune and match circuitry and a tube for balloon inflation. The tune and match circuitry

exits the rod at the proximal end of balloon at which point the loop coil originates which measures 7.0×3.5 cm^2. The trERC circuitry consists of fixed fcapacitors (ATC 100B Series, Huntington Station, NY) for matching and tuning with an additional 3 capacitors equally distributed around the coil to reduce local *E*-fields. The location and values of the capacitors are provided in Fig. 2a.

The roERC had the same basic geometry as the trERC but included a sleeve balun and both active and passive diodes to detune the ERC during RF transmission as it was used in combination with the trESA (28). The housing and flexibility of the inflatable ERC coil was found to limit the choices of the detune circuitry. We pursued a simple circuitry with minimal components that primarily achieves suppression of coil currents through a shift in resonance frequency. The actively switched diode (Microsemi Corporation, Irvine, CA, UM9401) created a short across the tune and match circuitry and shifted the ERC loop coil ~20 MHz off resonance during RF transmission. An additional passive cross-diode (Voltronics, Denville, NJ,MX51363-145) was used across the distributed capacitor at the top of the coil to detune the loop structure in the presence of induced currents in case of failure of the active diode. The modified coil circuitry is shown in Fig. 2b. The safety and effectiveness of this simplified detune circuitry was evaluated in phantom and in vivo studies.

All bench measurements required for coil tuning, matching, isolation and other circuit characterizations were performed using a calibrated Hewlet-Packard (Palo Alto, CA) HP 4396A network analyzer together with an 85046A “S” parameter test set. Specifically, coils were evaluated in terms of their reflectivity (S11), coupling (S12), unloaded quality factor (Q_0), and loaded quality factor (Q_L). Coil efficiency, C_{eff}, was then estimated by the standard relation ($C_{eff} = 1 - Q_L/Q_0$). Conditions of loading were obtained in vivo on a volunteer. Experimentally, in vivo DAM B_1^+ maps were generated to investigate the coupling between the ERC coils and the trESA.

Phantom Studies

Prior to in vivo use, each endorectal coil was tested and characterized with a phantom. This phantom consisted of a ~9L plastic (Nalge Nunc, Rochester NY) bottle filled with a solution of 4 mM $CuSO_4$ and 77 mM NaCl in deionized water. A 30 cm long plastic tube (Tuolox Plastics, Marion, IN) with an inside diameter of 4.45 cm and a wall thickness of 0.04 cm passed through and was attached to the lid of the larger plastic container with epoxy. The tube accepted the un-inflated ERC allowing it to be positioned near the center of the phantom. The coil was secured in position by inflating the balloon. This phantom setup allowed consistent positioning of the trERC and roERC coils for testing with and without the trESA.

B_1^+ mapping

Mapping of the transmit B_1 both in phantoms and in vivo was accomplished with the DAM approach (25) using a GRE acquisition with the following parameters: FOV = 160 to320 mm, TR = 6 s, TE = 4.1 ms, acquisition matrix = 128×96,slice thickness of 5 mm resulting in an acquisition time of 9.6 minutes per flip angle. Based on the two images acquired, the low flip angle, Θ, is estimated by $\arccos(|S_2(r)/2S_1(r)|)$, where $S_2(r)$ and $S_1(r)$ are the signal intensities from the higher and lower flip angles, respectively. The peak B_1^+ is subsequently calculated knowing the integral of the B_1^+ mapping RF pulse (I_{RF}) and its duration (t_{RF}) by the relationship $(\Theta * 2\pi) / (I_{RF} * t_{RF} * 360 * \gamma)$. This value is then scaled to report the peak B_1^+ assuming 1 W input power (B_{1_1W}) for each element of the transmit coil and the maximum B_1^+ (B_{1_max}) for the specific RF amplifiers and transmit chain used. All B_1^+

mapping and subsequent calculations were performed in IDL (ITT Visual Information Solutions, Boulder, CO, USA).

Receive and Parallel Imaging Performance

Receive and parallel imaging performance was calculated from an axial gradient echo acquisition acquired with the trESA+roERC with the following parameters: TR = 76 ms, TE = 3.8 ms, nominal flip angle 10° and a resolution of 1.3×1.3×10 mm3. To determine receive performance, the noise covariance matrix for each study, estimated from a separate noise scan, was used to decorrelate the roERC from the trESA. The remaining trESA elements were re-correlated and the SNR for the decorrelated roERC and the trESA were calculated independently using the pseudo-multiple replica method described by Robson et al. (29). Parallel imaging performance was evaluated by calculating geometry factors (*g*-factors) over ranges of accelerations in both the left-right and anterior-posterior directions (30). Average and maximum *g*-factors are then reported over the prostate and the region of the internal iliac artery. Both SNR and *g*-factor maps calculations were performed in Matlab (The Mathworks, Inc., Natick, MA, USA).

trESA Modeling

XFDTD, a finite difference time domain (FDTD) solver was used to evaluate coil performance and transmit power limits (REMCOM, Pittsburgh, PA). Coil performance measures included geometry factors, transmit B_1 (B_1^+) and receive B_1 (B_1^-) profiles. Transmit power limits were based on maintaining predicted local SAR limits below 8 W/kg averaged over one gram as recommended by the Center for Devices and Radiological Health within the U.S. Food and Drug Adminstration (FDA) (31).

Simulations were made in three-dimensions using a human body model consisting of a 5 mm cubical FDTD mesh generated from data from the Visual Human Project. Each tissue was characterized by its density, conductivity and permittivity. The trESA was simulated with and without the presence of the roERC. To incorporate the presence of the ERC, the human body model was modified by removing tissue posterior to the prostate to accommodate the space occupied by a fully inflated balloon. Both the trERC and the trESA coils were tuned to 297.2 MHz. When simulating the trESA, optimal phase based local B_1^+ shimming was performed for the region of the prostate as previously demonstrated (18). B_1^+ shimming provided the optimal transmit phases for each of the coil elements thus maximizing transmit efficiency when combined in the region of the prostate. These phases were used when performing the complex addition of the simulated B_1^+ and *E*-fields from each individual transmit element for the ESA in order to determine the final B_1^+ and SAR maps in the torso model. The simulated *B* and *E* fields were normalized to 1 W input power per channel for comparison with measured B_1^+ maps and determination of time averaged power limits based on calculated local peak SAR values. The simulated B_1^+ assumes close to an ideal coil with minimal losses. To more accurately represent experimental conditions, the transmit B_1 calculated by XFDTD are also scaled by the measured coil efficiencies, $(C_{\text{eff}})^{1/2}$.

At ultra-high fields, the application of RF over time is limited not by whole body average SAR but rather by local SAR (32). Therefore, in order to operate within FDA recommendations for local SAR of 8 W/kg per gram of tissue averaged over any 5 minute period, simulations were used to determine local peak SAR values normalized to 1 W input power per channel. The normalized peak SAR in 1 g of tissue (SAR_{peak_norm}) for a given coil was then converted to a limit on time averaged power ($TAP_{limit,coil}$) such that local SAR does not exceed the one gram averaged power of 8 W/kg by the relation

$$TAP_{limit,coil}=8\ W/kg\ ^{*}\ SAR_{peak\_norm}{}^{-1}\ ^{*}\ C_{eff}{}^{-1}. \quad [1]$$

Only power absorbed by the tissue can contribute to local *E*-fields, and thus SAR. Coil losses reduce the available power for generating electric as well as magnetic fields in the body. If the TAP_{limit} was exceeded, measures were taken to reduce the TAP by modifying RF pulses and/or adjusting other imaging parameters such as increasing repetition times or reducing the acquired slices.

trERC Modeling and Heating Studies

Simulations and heating experiments were performed with the trERC coil to validate acceptable power limits for in vivo use. Experimental safety testing was warranted for the trERC coil given the internal nature of this coil. For experimental testing, a cylindrical acrylic phantom with a 22 cm diameter and 20 cm long was filled with a polyacrylamide gel (6.5% acrylamide, 0.3% bisacrylamide, 0.05% TEMED, 0.08% ammonium persulfate; Fischer Scientific, Pittsburgh, PA) (33) constructed following the methods detailed by Bini et al. (34). The permittivity (73) and conductivity (0.79 S/m) were measured with an impedance/material analyzer (Agilent, Santa Clara, CA). The trERC was filled with perfluorocarbon and held in the center of the phantom during the polymerization process thus allowing the gel to completely surround the coil. Fiberoptic temperature probes (Luxtron Corp., Santa Clara, CA, USA) were positioned at 16 locations around the loop of the coil and feed circuitry including the feed point and the three distributed capacitors. Power was applied to the coil and forward and reflected power were monitored where the difference of the two was used to determine the input power to the coil. This input power would be equivalent to the power monitored during in vivo studies. The resulting input power applied to the trERC was a continuous 14.9 W for 10 minutes while temperatures were recorded at 1 s intervals. Local SAR in units of W/kg were calculated for compairson with simulation using the relation $dT/dt = SAR / c$, where dT is the difference in temperature over the initial linear part of the heating curve and c is the heat capacity of the gel estimated at ~ 4200 J/°C·kg (34).

Simulations of the trERC in the heating phantom setup were used to determine the expected *E*-field distribution for comparison with the heating studies, generation of B_1^+ profiles for comparison with in vivo measurements, and calculation of one gram averaged SAR for determination of $TAP_{limit,trERC}$. For the simulation, the trERC was modeled inside a uniform material with a 2 mm^3 resolution which was assigned the measured conductivity and permittivity values of the polyacrylamide gel.

In vivo MRI Studies

In vivo imaging data were collected on healthy volunteers under an IRB approved protocol. For the quantitative in vivo characterization of the coils, a single subject with a body mass index (BMI) of 22.3, height 1.62 m and weight 59 kg, was imaged with all three coil configurations. Results from this individual will be referred to as originating from the “reference volunteer”. In addition to the gradient echo acquisitions described above for B_1^+ mapping, shimming and evaluation of SNR and parallel imaging performance, anatomic T2w turbo spin echo (TSE) images were acquired to assess image quality obtainable from the 3 different coil configurations (TR 3500 ms, TE 130 ms, 3 mm slice thickness, 130 bandwidth per pixel, echo train length of 9 and a 220 mm FOV). A total of 10 slices with an acquisition time of 2:48 were acquired with a nominal in-plane resolution of 0.7 × 0.7 mm^2. For the combined trESA+roERC, higher resolution images (0.5 × 0.5 mm^2 in-place) were acquired by reducing the FOV to 160 mm while keeping all other parameters the same. In all

acquisitions, the phase encoding direction was in the left-right direction with 60% oversampling to avoid fold-over artifact on the prostate. To minimize the intense lipid signal immediately adjacent to the ESA and ERC coils on receive, a local volume was used for both B_0 shimming and center frequency determination allowing the effective use of a chemically shift selective saturation pre-pulse.

Subject Size Dependence

Both transmit and receive performance of the trESA were evaluated against subject size. Subject size was characterized by the width of the body from anterior to posterior ($AP_{distance}$) as determined from axial scout images at the level of the prostate. BMI values were also recorded and compared to $AP_{distance}$. In addition to the reference volunteer's B_1^+ information generated with the DAM method, four additional studies were performed in volunteers with varying body sizes. These B_1^+ maps were generated with the actual flip angle imaging technique which is a 3D gradient echo double TR approach (35). Results were comparable to the DAM values (36) with the added advantage of shorter acquisition times and volumetric coverage. The AFI sequence parameters included: FOV = 400 mm, TR1/TR2 = 20/120 ms, TE = 3.0 ms, acquisition matrix = 128×128, 18 slices and 3 mm slice thickness. The data for the two TR's were acquired in an interleaved manner resulting in a single acquisition of 4 minutes.

To investigate subject size dependence on receive performance, relative SNR maps were generated for eight additional subjects. Using a center profile normal to the plane of the roERC, the distance from the surface of the ERC at which the SNR of the trESA and roERC are equal ($rSNR1_{distance}$) was plotted against $AP_{distance}$.

RESULTS

Coil Characterization

The network analyzer results for coupling (S21) as well as loaded (Q_L) and unloaded (Q_0) quality factors are given in Table 1. The S21 values represent the average coupling between the trESA and each of the coil configurations under in vivo load. The coupling of the trESA with itself, −26.4±3.6 dB, is the average and standard deviation of the coupling between nearest neighbors on the anterior or posterior TEM arrays. When DC power is used to drive the diode in the roERC, the already low coupling between the trESA and the trERC of −36.2±5.3 dB is decreased to −48.0±6.1 dB.

However, since such port measurements do not allow for an evaluation of potential remaining local B_1 field effects due to imperfect decoupling, the loop structure under various states of detuning was also investigated. For this purpose, B_1^+ maps were generated in vivo with both the roERC and the trERC as receive only coils while transmitting with the trESA. As expected, there is residual coupling with the remaining off-resonant structure when the roERC's active diode was biased and even more so with the trERC (i.e. no detuning). In each configuration a new B_1^+ shim was determined and a B_1^+ map measured. The B_1^+ values in the region of the prostate for the trESA, trESA+roERC and trESA+trERC, with the trERC in receive-only mode, were 0.15±0.016, 0.18±0.027 and 0.26±0.054 $\mu T/W^{0.5}$, respectively. These B_1^+ measurements were compared against the performance of the trERC when using it as a transceiver coil as originally intended. The trERC as a transmit coil generated an average B_1^+ of 1.24 $\mu T/W^{0.5}$ in the prostate (Table 2). Therefore, coupling of the roERC with the trESA resulted in an increase which was 2.4% (0.18−0.15/1.24=0.024) of the B_1^+ when transmitting with the trERC. Coupling of the trERC, in receive-only mode, with the trESA resulted in an increase which was 9.6% (0.26−0.15/1.24=0.096) of the B_1^+ when transmitting with the trERC. Therefore, this translates to a 12 dB

($10\times\log_{10}[(0.024/0.096)^2]$) decrease in coupling when using the detuning circuitry of the roERC which experimentally validates the benchtop measurements.

Transmit and Receive Performance

Simulated and measured B_1^+ profiles through the prostate are shown for both the trERC and trESA in Fig. 3 and 4, respectively. For both the simulated and experimental values, the generated B_1^+ was scaled to 1 W input power (B_1_1W) per element. This corresponds to a total input power of 16 W for the 16 channel trESA and 1 W for the trERC. For simulation, the B_1^+ profiles are shown for the case of a nearly ideal coil with minimal losses (dashed curves) and scaled by the measured C_{eff} to account for losses realized experimentally (solid curves). The maximum achievable B_1^+ (B_1_max) for the investigated coils takes into consideration the peak output of the RF amplifiers and losses in the transmit chain. The losses from the RF amplifiers to the distribution panel at the back of the scanner is approximately 1 dB while from the back of the scanner to the coil is another 3.6 dB.

Summary statistics from the simulated and experimental results are provided in Table 2 from a prostate shaped region encompassing the profiles provided in Fig. 3 and 4. Along with the mean values, the B_1^+ distribution can be further appreciated by an estimate of B_1^+ inhomogeneity as given by the ratio of the standard deviation to the mean B_1^+ over the same regions. The inhomogeneity of the trESA from both simulation and in vivo results were 15% and 10%, respectively. The RF inhomogeneity of the trERC was 66% and 34% from simulation and experimental measurements, respectively. The difference in the simulated versus measured B_1^+ with the trERC is not surprising due to the limitations of the experimental technique and the extremely high B_1^+ close to the coil in vivo. The use of DAM to measure B_1^+ suffers from errors due to increasingly non-ideal slice profiles at the extremes in B_1^+. This can be appreciated further by the minimum and maximum values from each region and also partially explains the slightly higher mean B1+ from simulation.

With the trESA, transmit efficiency associated with B_1^+ shimming as determined by the fractional available B_1^+ also needs to be considered and is typically around 85% for prostate studies in vivo (18). In this case, the fractional available B_1^+ realized in the prostate was 0.84 in simulation and 0.88 experimentally which means that 84% and 88% of the RF constructively interferes over the region of the prostate.

Receive B_1 values in vivo from the reference volunteer from approximately the same locations are shown in Fig. 5 for all three coil configurations: trESA, trERC and trESA +roERC. The ERC coil performs approximately 5 times better on receive than the trESA close to the rectum while the distance from the surface of the ERC at which the SNR of the trESA and roERC are equal ($rSNR1_{distance}$) was 2.8 cm based on the profile given in Fig. 5a. The vertical SNR profile was taken from the middle of the prostate which is over 6 mm anterior to the plane of the loop element in the ERC due to the inflation of the coil's balloon. In general, the SNR will favor the ERC more if the profile is taken further to the right and less with a profile further to the left as evidenced by the SNR taken horizontally as shown in Fig. 5b.

Coil Dependent TAP limits

A representative axial slice of the 3D body model with the trESA and the void resulting from the ERC coil balloon is shown in Fig. 6a. An image of the SAR is shown in Fig. 6b at the location of peak SAR. The peak 1 g average SAR (SAR_{peak_norm}) in the body was 6.29 W/kg. Using SAR_{peak_norm}, the $TAP_{limit,trESA}$ is equal to 2.54 W based on Equation 1.

The TAP limit for the trERC, $TAP_{limit,trERC}$, was determined from simulation and heating experiments in the gel phantom. From the 16 locations tested in the heating experiments,

maximum heating and SAR occurred adjacent to the feed point of the coil and the first distributed capacitor as indicated by the horizontal and vertical arrows respectively in Fig. 6c and 6d. The heating curves at these locations are shown in Fig. 6e. For an input power of 13.4 W, the temperature at the first distributed capacitor and the feed point increased 9.9 °C over 10 minutes. Despite the similarities in maximum temperature at the 10 minute mark, the probe at the distributed capacitor measured the highest SAR of 12.4 W/kg normalized to one Watt. The peak SAR determined in the phantom simulation was 13.6 W/kg in a single 2×2×2 mm^3 cell which is consistent with the point source value calculated in the heating experiment providing confidence in the simulated results. The one gram averaged SAR_{peak_norm} determined from simulation was 6.64 W/kg resulting in a $TAP_{limit,trERC}$ of 1.34 W based on Equation 1. Both the SAR_{peak_norm} and TAP_{limit} are summarized in Table 2.

Parallel Imaging Performance

As parallel imaging plays an important part in improved spatial and temporal resolution of dynamic contrast enhanced imaging studies, mean *g*-factors were calculated over the prostate and the region of the major feeding vessels typically used to obtain an arterial input function. As shown in Table 3, the trESA performs well, exhibiting low *g*-factors in both the region of the prostate and the artery with a range of reduction factors along the left-right and anterior-posterior directions. With the inclusion of the roERC, there is only a modest increase in parallel imaging performance in the prostate with little or no observable difference in the region of the artery which is far from the roERC. These in vivo results are supported by similar *g*-factors calculated from simulated data in the region of the prostate (data not shown).

Anatomic Imaging Studies

Fig. 7 shows T2w anatomic images from the reference volunteer at nearly the same level of the prostate obtained in different imaging sessions with each of the three coil configurations. The full FOV images are shown in the top row (Fig. 7a) while the same images zoomed in to the region of the prostate in the lower row (Fig. 7b). There are two data sets shown for the trERC coil. The trERC-low image is acquired with a lower power setting more appropriate for achieving the desired T2 contrast close to the coil at the expense of under exciting spins on the anterior side of the gland as indicated by the horizontal arrow. The trERC-high data is acquire with three times as much power as the trERC-low in order to generate a sufficient B_1^+ in the anterior portion of the prostate at the expense of over-flipping spins close to the coil as shown by the vertical arrow. The trESA+roERC image shows consistent contrast throughout the prostate as with the trESA alone with the added advantage of improved SNR close to the rectum. Taking advantage of the increased SNR of the combined coil, the images in Fig. 8 show the transverse, sagittal and coronal views of the prostate with an in-plane resolution of 0.5 × 0.5 mm^2. This data was acquired by reducing the FOV to 160 mm while keeping all parameters the same as the images in Fig. 7.

Subject Size Dependence

The relationship between transmit and receive performance as a function of $AP_{distance}$ are shown in Fig. 9. For the 13 subjects included in these comparisons, BMI and $AP_{distance}$ were highly correlated with the following estimated relationship: $BMI = 1.56\times AP_{distance} - 6.6$ with $R^2=0.93$. Therefore, in this study, an $AP_{distance}$ of 22.1 cm will be used to represent the average size adult male in the U.S. which corresponds to average BMI reported by the CDC of 27.9 (37). For the reference volunteer the $AP_{distance}$ was 19.0 cm. B_1^+ was found to be inversely correlated to $AP_{distance}$ by the relation $B_1^+(\mu T/W^{0.5}) = -1.17\times10^{-2}\times AP_{distance}+0.380$ with $R^2= 0.73$. Based on this relationship, a B_1^+ of 0.122 μT/

$W^{0.5}$ is expected for the average adult male with the trESA; a decrease of 20% from the reference volunteer.

A positive, linear correlation was determined between $rSNR1_{distance}$ and $AP_{distance}$ as given by the relation $rSNR1_{distance} = 0.266 \times AP_{distance} - 2.03$ with $R^2 = 0.75$. For the average adult male, $rSNR1_{distance}$ is equal to 3.8 cm which is an increase of 36% over that of the reference volunteer.

DISCUSSION

On closed bore clinical scanners, a body coil is typically used to generate a relatively homogenous transmit RF field while local receive arrays are typically used for reception. However, whole body transmit coils, standard on most clinical scanners, become increasingly challenging for applications at 7 Tesla resulting from increased power absorption and decreased wavelengths. Even though the feasibility of whole body RF coils has been demonstrated at high fields including 4T (38) and 7T (39), the limits on maximum peak transmit B_1 and strong field inhomogeneity have not yet been adequately addressed for general use. The decreased efficiency and homogeneity at high field is a result of destructive interferences exacerbated by the short wavelengths in tissue at 300 MHz (~12 cm) (40).

Along with destructive interferences, increased power deposition which is proportional to B_0^2 decreases the available power to generate B_1^+ at 7T. That is, a greater percentage of the power transmitted into the body is absorbed by the tissue in the form of *E*-fields resulting in heating. The *E*-field distribution in the body is complex and results from destructive/constructive interferences plaguing B_1^+ and is greatly influenced by the distribution of tissues with widely varying electrical properties such as fat and muscle (41). This can be seen in the simulated SAR maps of the trESA coil, Fig. 6b. The *E*-fields track the conductive structures in the body resulting in peak SAR in the skin and muscle. The presence of tremendous *E*-field and thus SAR inhomogeneity in the body disallows the use of whole body averaged SAR as a criteria for determining safe limits of operation. Instead, local SAR or temperature increases are used to determine limits on time averaged power for a given coil configuration. This can be determined through simulation or through experimental heating studies as demonstrated in this paper and by others (22).

A partial solution to the practical limits of field homogeneity, peak B_1^+ and SAR management associated with the use of whole body RF coils at high field involves the use of smaller or local transmit coils, either as transceivers or transmit only designs. Combining this local coil strategy with B_1^+ shimming greatly improves head imaging and makes body imaging possible (18). However, issues with achieving sufficient B_1^+ for certain acquisitions such as spectroscopy still persist even with local transceiver arrays. The use of adiabatic pulses can be used to obtain the high bandwidth RF pulses required to minimize chemical shift displacement in spectroscopy studies even with low peak B_1^+ performance ((42) and references therein) however, the increasing pulse lengths and high local SAR become a limiting factor. In conjunction with adiabatic pulses or by itself, the variable rate selective excitation (VERSE) technique may also help address limitations in peak B_1^+, but comes at the expense of poor off-resonance performance (19,43).

The local trESA transceiver array characterized in this paper was able to generate a B_1^+ 0.152 $\mu T/W^{0.5}$ in general with a system specific maximum B_1^+ of 11.9 μT using the current RF amplifiers and cabling in the reference volunteer. This performance is achieved after using a B_1^+ shimming method optimizing for transmit efficiency. Using B_1^+ shimming to optimize B_1^+ homogeneity over the whole prostate area would greatly reduce the achievable B_1^+ even further. Even though homogeneity was not a goal of the type of B_1^+ shimming

performed, B_1^+ in homogeneity was only 10% (ratio of standard deviation to mean B_1^+) after B_1^+ shimming over the region of the prostate and typically performs at least this well as previously reported (18).

The trERC coil provides improved peak transmit and receive B_1 but at the expense of reduced homogeneity compared to the trESA. With respect to B_1^- in the reference volunteer, the trERC exhibits approximately a 5-fold advantage near the loop coil compared to the trESA and has an $rSNR1_{distance}$ of 2.8 cm. While trERC receive inhomogeneity results in correctable display issues, the most deleterious effects originate from the inhomogeneous transmit B_1 which was measured at 34% in vivo and 66% in simulation. For reasons previously explained, the simulated inhomogeneity is most likely closer to what is actually being realized in vivo. As shown in the vertical and horizontal profiles in Fig. 4, the B_1^+ inhomogeneity is not only dependent on the distance normal to the coil but is also asymmetric across the coil from left to right. As shown in Fig. 7, the B_1^+ inhomogeneity of the trERC makes it difficult to achieve a uniform contrast across the entire prostate. Close to the coil, B_1^+ insensitive adiabatic pulses can be used to achieve good localization in spectroscopic studies as previously demonstrated by Klomp et al. (22). For T2w imaging however, a previously presented adiabatic RARE sequence (44) is acknowledged to have a much high power deposition than the TSE sequence used in this study which was already close to the allowable local SAR limit. Again, combining adiabatic RARE with SAR reduction strategies such as VERSE may help mitigate these issues to a level sufficient to allow reasonable anatomic imaging.

When attempting to cover the entire prostate the limited peak B_1^+ again becomes a factor even with the trERC. In the reference volunteer, the trERC decreases from a maximum of 1.8 $\mu T/W^{0.5}$ at the posterior margin of the prostate near the coil at the midline, to 0.4 $\mu T/W^{0.5}$ at a distance of 3cm. From the anterior midline through the right anterior quadrant of the prostate, the average B_1^+ generated by the trESA is approximately equivalent to or greater than that generated by the trERC even when considering the reduced performance in a larger average size adult male. Furthermore, the B_1^+ distribution of the trERC is highly dependent on the rotation of the coil which is not easy to accurately adjust in vivo with the balloon-type coil currently used.

The trESA+roERC coil combines several benefits of both coils and has resulted in the best anatomic imaging of the prostate to date at 7T as shown in Fig. 8. Combining the roERC with the trESA improves the imaging of critical structures such as the posterior prostate capsule, neurovascular bundle, and peripheral zone in several ways. First, the trESA provides a homogeneous B_1^+ resulting in uniform contrast across the prostate. Meanwhile, the roERC increases receive sensitivity, reduces prostate/rectum motion and allows control over susceptibility by filling the coil balloon with a perfluorocarbon. The challenge with this configuration is the same as the trESA coil alone, a relatively low peak B_1^+.

TAP determination

The SAR limits for the trESA were chosen based on simulation as opposed to heating measurements for several reasons. First, temperature measurements in vivo are impractical as the location of maximum heating is at first unknown making it difficult to accurately place probes on the surface and unreasonable to place probes subcutaneously. Second, it is difficult to build a phantom to reasonably approximate the widely varying tissue properties which have a tremendous effect on *E*-field distributions. Finally, the multi-channel transmitter further complicates the issue as there are complex *E*-fields generated by each transmit element which constructively and destructively interfere. The situation is similar to the issues faced with B_1^+ but additionally complicated by the influence of tissue boundaries and varying electrical properties. Therefore, in order to incorporate this complexity, the

human body model was used in simulations accepting its overall size and shape would differ from in vivo measurements.

To determine TAP limits for the trERC, the phantom study was most appropriate as it allowed both simulation and experimental testing. Experimentally, the phantom allowed interrogation of the temperature at multiple locations in the polyacrylamide gel immediately adjacent to the coil. Along with simulation, it was deemed important with this internal coil to measure the maximum local heating along the conductor which, except for a latex balloon, is immediately adjacent to the tissue. Temperature measurements confirmed simulation results that the location of maximum heating occurs directly above the capacitors (Fig. 6e), and the resulting local SAR measurements from the heating study were similar to the local SAR predicted in the phantom model from a single cell in the simulation. These results along with similar B_1^+ profiles in both simulation and in vivo, gave confidence in the calculation of $TAP_{limit,trERC}$ from the simulated SAR_{peak_norm}.

Limitations on Transmit B $_1$

Considering the local SAR constraint alone, more power can be used for the trESA than for the trERC by the factor $TAP_{limit,trESA}/TAP_{limit,trERC} = 2.54/1.34 = 1.9$. Despite this apparent advantage, the average B_1^+ in the prostate is still lower for the trESA than the trERC. For demonstration purposes, assuming we are at the SAR limit with 1 W input power for the trERC, the trESA could use 1.9 W. Therefore, for the reference volunteer, the trESA coil could generate a relative field of $0.152\times(16\times1.9)^{0.5} = 0.84$ μT compared to the average trERC value of 1.24 μT. In the average male, the generated field by the trESA would be reduced by 20% compared to the reference volunteer resulting in a B_1^+ of 0.67 μT.

In reality however, there is a finite amount of power available to generate B_1^+ especially in the case of the trESA. This limit is a function of the power rating and performance of the amplifiers, losses in the cables and connections from the amplifier to the coil as well as the coil match and efficiency. For the specific system used in this study, the maximum achievable B_1^+ (B_1_max) in Fig. 3 and 4 for the reference volunteer corresponds to the maximum possible output of our RF amplifiers. In this power limited case, as presented in Fig. 3 and 4, the maximum B_1^+ of the trESA was 11.9 μT for the reference volunteer which would correspond to an B_1^+ of 9.3 μT in the average adult male. In comparison, starting with a single 1 kW amplifier the maximum achievable B1+ achieved for the trERC averaged over the prostate was 24.2 μT.

Parallel Imaging Performance

It has been previously demonstrated that the 16 channel stripline array used in this work performs quite well for parallel imaging across the entire human torso (27,45). In this study, local *g*-factors were determined in the prostate and external iliac artery as these locations are the most relevant for prostate DCE-MRI studies. Even at the location of its maximum contribution in receive B_1, the roERC only modestly improves *g*-factors and this benefit is seen primarily in the anterior-posterior direction. In the artery, where the contribution of the trERC is much less, there is almost no difference when compared with the trESA alone as would be expected. It is important to mention that if the AIF from the external iliac artery is desired for pharmacokinetic modeling, then using a trESA or at least a local transmit coil is an absolute requirement. On the receive side, improving local parallel imaging of the prostate could be improved further in this configuration through the use of longitudinal (46) and horizontal (47) ERC arrays.

Coil Design Considerations

The current roERC was a first attempt to provide a safe coil for in vivo use which fit the form factor of the available commercial housing and provided high quality images of the prostate. The first step in its design involved testing various configurations with a primary focus on understanding and mitigating coupling with the trESA for both reasons of safety and image quality. While the regional B_1^+ perturbations were in a large part manageable with B_1^+ shimming methods, even in the case of the trERC, there were induced fields close to the coil which resulted in poor image quality (B_1 components) and potentially local heating (E components). Therefore, the goal was to mitigate these induced fields. The in vivo studies demonstrated that the current roERC significantly improves receive performance and minimally impacts B1+ homogeneity when combined with local B_1^+ phase shimming.

With a modification of the current coil design there is the potential to further exploit inductive coupling to augment the local B_1^+ performance in the region of the prostate. Such methods have been previously published to increase local transmit B1 in the body and head (48,49). Some of these effects were observed in the data presented in the coil characterization results. When transmitting with the trESA and using the roERC and trERC as receive only coils, the average transmit B1 in the prostate increased, 20% and 73%, respectively. While not unexpected, the current coil design was not specifically designed for this purpose and is an area for future investigation.

CONCLUSIONS

Three different coil configurations to investigate the prostate at 7 Tesla were compared in this study: a transceiver ERC coil (trERC), a 16 channel transceiver external surface array (trESA) and a trESA combined with a receive only ERC (roERC) be referred to as trESA +roERC. The advantages of the trERC are higher peak B_1^+ performance, improved SNR, the ability to perform reduced FOV imaging, decreased prostate motion and control over susceptibility mismatches with the rectum, better visualization of the neurovascular bundle and patient size independent performance. Our results suggest that trERC could play a significant role in cases where peak B_1^+ value is the most critical factor at least close to the coil, such as in spectroscopic studies. However, the B_1^+ asymmetry across the coil and rapid decrease of B_1^+ with increasing distance from the coil limit the advantage of the peak B_1^+ performance and compromise anatomic and other functional imaging studies. The trESA benefits from B_1^+ and B_1^- homogeneity over the prostate area, increased anatomical coverage, capability of performing both parallel transmit and receive methods along with improved patient acceptance. However, in its current implementation the trESA configuration is limited in power on the transmit side and in SNR on the receive side. The trESA+roERC coil combines many of the best attributes of each such as the trESA's homogenous B_1^+ and parallel imaging performance along with the ERC's superior SNR to obtain optimal image quality. Another limiting factor for both the trESA and the combined trESA+roERC is the subject size dependent available B_1^+ in the prostate that decreases as the coil elements move further away from the target anatomy. Improving transmit chain and coil efficiency in the trESA configuration would further extend the promise of the trESA +roERC for prostate studies.

Acknowledgments

Funding for this work was provided by the National Institutes of Health (NIH) grants P41-RR008079, R01-EB000895-04, R01-EB007327, M01-RR00400 and R01-CA131013. The original acquisition of the 7 Tesla system was funded by the Keck Foundation. We would also like to acknowledge Chris Collins (Penn State University, Hershey, PA) and his group for providing permittivity and conductivity characteristics for the phantom studies,

Jinfeng Tian (University of Minnesota, Minneapolis, MN) for useful discussion on FDTD simulations and Rajesh Venkataraman (University of Minnesota, Minneapolis, MN) for assistance with data analysis.

REFERENCES

1. Shukla-Dave A, Hricak H, Kattan MW, Pucar D, Kuroiwa K, Chen HN, Spector J, Koutcher JA, Zakian KL, Scardino PT. The utility of magnetic resonance imaging and spectroscopy for predicting insignificant prostate cancer: an initial analysis. BJU Int. 2007; 99(4):786–793. [PubMed: 17223922]
2. Haider MA, Chung P, Sweet J, Toi A, Jhaveri K, Menard C, Warde P, Trachtenberg J, Lockwood G, Milosevic M. Dynamic contrast-enhanced magnetic resonance imaging for localization of recurrent prostate cancer after external beam radiotherapy. Int J Radiat Oncol Biol Phys. 2008; 70(2):425–430. [PubMed: 17881141]
3. Coakley FV, Kurhanewicz J, Lu Y, Jones KD, Swanson MG, Chang SD, Carroll PR, Hricak H. Prostate cancer tumor volume: measurement with endorectal MR and MR spectroscopic imaging. Radiology. 2002; 223(1):91–97. [PubMed: 11930052]
4. Claus FG, Hricak H, Hattery RR. Pretreatment evaluation of prostate cancer: role of MR imaging and 1H MR spectroscopy. Radiographics. 2004; 24(Suppl 1):S167–180. [PubMed: 15486239]
5. Reinsberg SA, Payne GS, Riches SF, Ashley S, Brewster JM, Morgan VA, deSouza NM. Combined use of diffusion-weighted MRI and 1H MR spectroscopy to increase accuracy in prostate cancer detection. AJR Am J Roentgenol. 2007; 188(1):91–98. [PubMed: 17179350]
6. Bloch BN, Rofsky NM, Baroni RH, Marquis RP, Pedrosa I, Lenkinski RE. 3 Tesla magnetic resonance imaging of the prostate with combined pelvic phased-array and endorectal coils; Initial experience(1). Acad Radiol. 2004; 11(8):863–867. [PubMed: 15288036]
7. Futterer JJ, Scheenen TW, Huisman HJ, Klomp DW, van Dorsten FA, Hulsbergen-van de Kaa CA, Witjes JA, Heerschap A, Barentsz JO. Initial experience of 3 tesla endorectal coil magnetic resonance imaging and 1H-spectroscopic imaging of the prostate. Invest Radiol. 2004; 39(11):671–680. [PubMed: 15486528]
8. Metzger, G.; Ocak, I.; Bernardo, M.; Choyke, P. Quantification of prostate spectra at 3T using LCModel with a simulated basis set; Proceedings of the 15th Annual Meeting of ISMRM; Berlin, Germany. 2007. p. 802
9. Swanson MG, Vigneron DB, Tabatabai ZL, Males RG, Schmitt L, Carroll PR, James JK, Hurd RE, Kurhanewicz J. Proton HR-MAS spectroscopy and quantitative pathologic analysis of MRI/3D-MRSI-targeted postsurgical prostate tissues. Magn Reson Med. 2003; 50(5):944–954. [PubMed: 14587005]
10. Henderson E, Rutt BK, Lee TY. Temporal sampling requirements for the tracer kinetics modeling of breast disease. Magn Reson Imaging. 1998; 16(9):1057–1073. [PubMed: 9839990]
11. Wiesinger F, Van de Moortele PF, Adriany G, De Zanche N, Ugurbil K, Pruessmann KP. Parallel imaging performance as a function of field strength--an experimental investigation using electrodynamic scaling. Magn Reson Med. 2004; 52(5):953–964. [PubMed: 15508167]
12. Sosna J, Pedrosa I, Dewolf WC, Mahallati H, Lenkinski RE, Rofsky NM. MR imaging of the prostate at 3 Tesla: comparison of an external phased-array coil to imaging with an endorectal coil at 1.5 Tesla. Acad Radiol. 2004; 11(8):857–862. [PubMed: 15354305]
13. Futterer JJ, Heijmink SW, Scheenen TW, Jager GJ, Hulsbergen-Van de Kaa CA, Witjes JA, Barentsz JO. Prostate cancer: local staging at 3-T endorectal MR imaging--early experience. Radiology. 2006; 238(1):184–191. [PubMed: 16304091]
14. Hoult DI, Phil D. Sensitivity and power deposition in a high-field imaging experiment. J Magn Reson Imaging. 2000; 12(1):46–67. [PubMed: 10931564]
15. Kaji Y, Kuroda K, Maeda T, Kitamura Y, Fujiwara T, Matsuoka Y, Tamura M, Takei N, Matsuda T, Sugimura K. Anatomical and metabolic assessment of prostate using a 3-Tesla MR scanner with a custom-made external transceive coil: healthy volunteer study. J Magn Reson Imaging. 2007; 25(3):517–526. [PubMed: 17279524]
16. Kim HW, Buckley DL, Peterson DM, Duensing GR, Caserta J, Fitzsimmons J, Blackband SJ. In vivo prostate magnetic resonance imaging and magnetic resonance spectroscopy at 3 Tesla using a

transceive pelvic phased array coil: preliminary results. Invest Radiol. 2003; 38(7):443–451. [PubMed: 12821859]

17. Pinkerton RG, Near JP, Barberi EA, Menon RS, Bartha R. Transceive surface coil array for MRI of the human prostate at 4T. Magn Reson Med. 2007; 57(2):455–458. [PubMed: 17260367]
18. Metzger GJ, Snyder C, Akgun C, Vaughan T, Ugurbil K, Van de Moortele PF. Local B(1) (+) shimming for prostate imaging with transceiver arrays at 7T based on subject-dependent transmit phase measurements. Magn Reson Med. 2008; 59(2):396–409. [PubMed: 18228604]
19. Near J, Romagnoli C, Bartha R. Reduced power magnetic resonance spectroscopic imaging of the prostate at 4.0 Tesla. Magn Reson Med. 2009; 61(2):273–281. [PubMed: 19165876]
20. Metzger GJ, Snyder CJ, Akgun C, Adriany G. Comparison of Transceive Endorectal and External Surface Array Coils for Prostate Imaging at 7 Tesla. Proc Intl Soc Mag Reson Med. 2008; 16:171.
21. Klomp D, Bitz AK, Heerschap A, Scheenen TW. Proton Spectroscopic Imaging of the Human Prostate in Vivo at 7T. Proc Intl Soc Magn Reson in Med. 2008; (16):1598.
22. Klomp DW, Bitz AK, Heerschap A, Scheenen TW. Proton spectroscopic imaging of the human prostate at 7 T. NMR Biomed. 2009; 22(5):495–501. [PubMed: 19170072]
23. Vaughan, JT.; Adriany, G.; Strup, J.; Andersen, P.; Ugurbil, K.; Massachusetts General Hospital, assignee. Parallel tranceiver for nuclear magnetic resonance systems. 2005. USA patent 6,633,161
24. Vaughan T, DelaBarre L, Snyder C, Tian J, Akgun C, Shrivastava D, Liu W, Olson C, Adriany G, Strupp J, Andersen P, Gopinath A, van de Moortele PF, Garwood M, Ugurbil K. 9.4T human MRI: preliminary results. Magn Reson Med. 2006; 56(6):1274–1282. [PubMed: 17075852]
25. Insko E, Bolinger L. Mapping of the radiofrequency field. J Magn Reson. 1993; 103:82–85. Series A.
26. Vaughan, JT.; Massachusetts General Hospital, assignee. RF coil for imaging system. 2003. USA patent 6,633,161
27. Snyder, CJ.; DelaBarre, L.; Van de Moortele, PF.; Snyder, A.; Akgun, C.; Jinfeng, T.; Metzger, G.; Ugurbil, K.; Vaughan, JT. Stripline/TEM Transceiver Array for 7T Body Imaging; Proceedings of the 15th Annual Meeting of ISMRM; Berlin, Germany. 2007. p. 164
28. Metzger GJ, Moeller S, Snyder CJ, Ugurbil K, Van de Moortele PF, Adriany G. Endorectal combined surface array for prostate imaging at 7T. Proc Intl Soc Mag Reson Med. 2009; 17:#6038.
29. Robson PM, Grant AK, Madhuranthakam AJ, Lattanzi R, Sodickson DK, McKenzie CA. Comprehensive quantification of signal-to-noise ratio and g-factor for image-based and k-space-based parallel imaging reconstructions. Magn Reson Med. 2008; 60(4):895–907. [PubMed: 18816810]
30. Pruessmann KP, Weiger M, Scheidegger MB, Boesiger P. SENSE: sensitivity encoding for fast MRI. Magn Reson Med. 1999; 42(5):952–962. [PubMed: 10542355]
31. CDRH. Services DoHaH. Criteria for Significant Risk Investigations of Magnetic Resonance Diagnostic Devices. 2003
32. Center for Devices and Radiological Health. Criteria for Significant Risk Investigations of Magnetic Resonance Diagnostic Devices. U.S. Department of Health and Human Services Food and Drug Administration; 2003.
33. Yeung CJ, Karmarkar P, McVeigh ER. Minimizing RF heating of conducting wires in MRI. Magn Reson Med. 2007; 58(5):1028–1034. [PubMed: 17969097]
34. Bini MG, Ignesti A, Millanta L, Olmi R, Rubino N, Vanni R. The polyacrylamide as a phantom material for electromagnetic hyperthermia studies. IEEE Trans Biomed Eng. 1984; 31(3):317–322. [PubMed: 6715003]
35. Yarnykh VL. Actual flip-angle imaging in the pulsed steady state: a method for rapid three-dimensional mapping of the transmitted radiofrequency field. Magn Reson Med. 2007; 57(1):192–200. [PubMed: 17191242]
36. Malik SJ, Larkman DJ, Hajnal JV. Optimal linear combinations of array elements for B1 mapping. Magn Reson Med. 2009; 62(4):902–909. [PubMed: 19658161]
37. Ogden, CL.; Fryar, CD.; Carroll, MD.; Flegal, KM. Advance data from vital and health statistics; no 347. National Center for Health Statistics; Hyattsville, Maryland: 2004. Mean body weight, height, and body mass index, United States 1960-2002.

38. Vaughan JT, Adriany G, Snyder CJ, Tian J, Thiel T, Bolinger L, Liu H, DelaBarre L, Ugurbil K. Efficient high-frequency body coil for high-field MRI. Magn Reson Med. 2004; 52(4):851–859. [PubMed: 15389967]
39. Vaughan JT, Snyder CJ, DelaBarre LJ, Bolan PJ, Tian J, Bolinger L, Adriany G, Andersen P, Strupp J, Ugurbil K. Whole-body imaging at 7T: preliminary results. Magn Reson Med. 2009; 61(1):244–248. [PubMed: 19097214]
40. Van de Moortele PF, Akgun C, Adriany G, Moeller S, Ritter J, Collins CM, Smith MB, Vaughan JT, Ugurbil K. B(1) destructive interferences and spatial phase patterns at 7 T with a head transceiver array coil. Magn Reson Med. 2005; 54(6):1503–1518. [PubMed: 16270333]
41. Hand JW, Lagendijk JJ, Hajnal JV, Lau RW, Young IR. SAR and temperature changes in the leg due to an RF decoupling coil at frequencies between 64 and 213 MHz. J Magn Reson Imaging. 2000; 12(1):68–74. [PubMed: 10931565]
42. Tannus A, Garwood M. Adiabatic pulses. NMR Biomed. 1997; 10(8):423–434. [PubMed: 9542739]
43. Gai ND, Zur Y. Design and optimization for variable rate selective excitation using an analytic RF scaling function. J Magn Reson. 2007; 189(1):78–89. [PubMed: 17889579]
44. de Graaf RA, Rothman DL, Behar KL. Adiabatic RARE imaging. NMR Biomed. 2003; 16(1):29–35. [PubMed: 12577295]
45. Snyder CJ, DelaBarre L, Metzger GJ, van de Moortele PF, Akgun C, Ugurbil K, Vaughan JT. Initial results of cardiac imaging at 7 Tesla. Magn Reson Med. 2009; 61(3):517–524. [PubMed: 19097233]
46. Kim DY, Schnall MD, Rosen MA, Connick T. Prostate MR imaging at 3T with a longitudinal array endorectal surface coil and phased array body coil. J Magn Reson Imaging. 2008; 27(6): 1327–1330. [PubMed: 18504745]
47. Yung AC, Oner AY, Serfaty JM, Feneley M, Yang X, Atalar E. Phased-array MRI of canine prostate using endorectal and endourethral coils. Magn Reson Med. 2003; 49(4):710–715. [PubMed: 12652542]
48. Schmitt M, Feiweier T, Voellmecke E, Lazar R, Krueger G, Reykowski A. B1-Homogenization in abdominal imaging at 3T by means of coupling coils. Proc Intl Soc Mag Reson Med. 2005; 13:331.
49. Wiggins GC, Zakszewski E, Wiggins CJ, Wald LL. B1 Transmit Field Manipulation at 7 Tesla Using Controlled Decoupling of Array Coil Elements (CODACE). Proc Intl Soc Mag Reson Med. 2007; 15:1054.

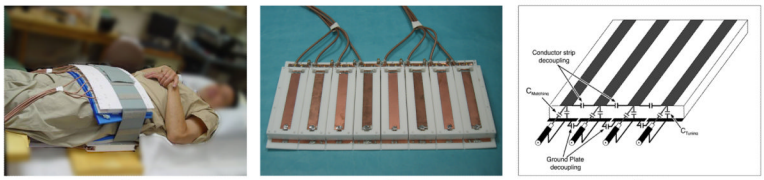

Figure 1.
(a) The 16 channel external surface array (ESA) consisted of two 8-element TEM arrays positioned anterior and posterior to the pelvis. (b) The anterior array with the patient side PTFE plate removed showing the copper strip conductors on top. (c) A schematic of a 4 channel version of the TEM array demonstrating the relative positioning of the tuning, matching and decoupling capacitors.

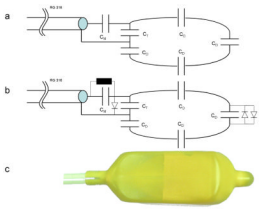

Figure 2.
The ERC circuitry consisted of 6 capacitors for matching, tuning and distributing currents around the coil. The tune and match circuitry exits the rod at the proximal end of balloon at which point the loop coil originates which measures 7 cm long and 3 cm wide. The trERC coil (a) used the following matching, tuning and distributed capacitor values respectively: C_M=12 pF, C_T=8.2 pF and C_D=8.2 pF. The roERC (b) has a similar configuration but with an active diode to create a short across the tune and match circuitry and a passive cross-diode across the distributed capacitor at the tip to detune the loop structure in the presence of induced currents. With the addition of the diodes, the roERC required slightly different capacitor values: C_M=10 pF , C_T=9.1pF and C_D=8.2pF. (c) The completed coil after stretching the original latex cover over the inner balloon and modified electronics.

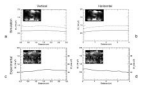

Figure 3.
B_1^+ profiles for the trESA. The line within each plots inset picture shows the location at which the profile was obtained. Vertical profiles from simulation (a) and measurement (c) from the middle of the prostate starting from the rectal wall and extending 3 cm anteriorly. Horizontal profiles from simulation (b) and measurement (d) approximately parallel and 1 cm away from the most anterior aspect of the rectum. All profiles are scaled to 1W input power per element corresponding to a total input power of 16 W for the trESA. Simulated data (a) and (b) show both the original calculated B_1^+ profiles (broken curve) and the B_1^+ scaled by coil efficiency C_{eff} (solid curve). Experimental profiles (c) and (d) are also scaled for maximum achievable B_1^+ (B_1_max) with the currently available transmit chain.

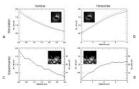

Figure 4.
B_1^+ profiles for the trERC. The line within each plots inset picture shows the location at which the profile was obtained. Vertical profiles from simulation (a) and measurement (c) from the middle of the prostate starting from the rectal wall and extending 3 cm anteriorly. Horizontal profiles from simulation (b) and measurement (d) approximately parallel to surface of the trERC and 1 cm in from the most anterior aspect of the rectum. All profiles are scaled to 1W input power. Simulated data (a) and (b) show both the original calculated B_1^+ profiles (broken curve) and the B_1^+ scaled by coil efficiency C_{eff} (solid curve). Experimental profiles (c) and (d) are also scaled for maximum achievable B_1^+ (B_1_max) with the currently available transmit chain.

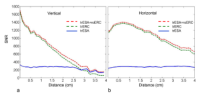

Figure 5.
(a) Vertical and (b) horizontal SNR profiles from the trESA (blue curve), roERC (broken green curve) and combined trESA+roERC (broken red curve). The data were obtained from the in vivo experimental SNR acquisition. Vertical profiles were taken from the middle of the prostate starting from the boundary between the rectum and prostate and extending 3 cm anteriorly. Horizontal profiles were taken approximately 1 cm away and parallel to the rectum.

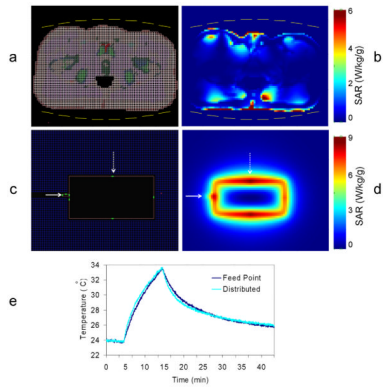

Figure 6.

(a) A single axial slice from the 3D FDTD model with the void created by the ERC's balloon and the position of the 16 elements of the trESA coil. (b) An axial cross section at the point of maximum SAR for the trESA coil with 5×5×5 mm^3 resolution. (c) Coronal section of the trERC model in the polyacrylamide gel phantom at the level of the coil. (d) Coronal slice of calculated SAR 4 mm above the trERC coil with a resolution of 2×2×2 mm^3. (e) The heating curves during 10 minutes of heating with 13.4 W continuous power at the point of the feed and distributed capacitors as indicated on by the solid and dashed arrows respectively in (c) and (d).

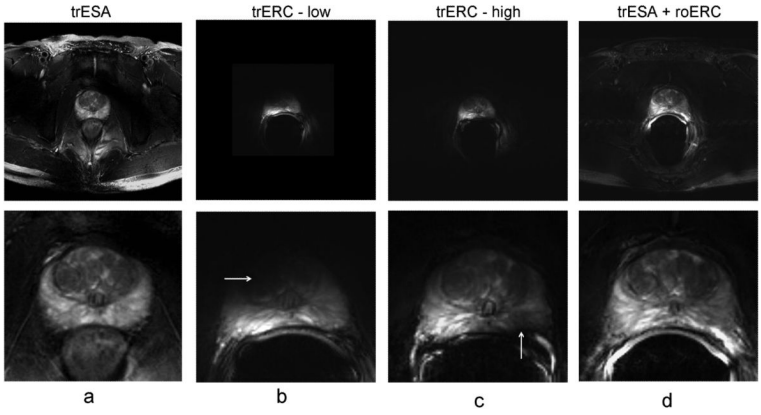

Figure 7.
Full field-of-view axial T2w-TSE images (upper row) and zoomed images (lower row) of the prostate with the (a) trESA, (b) trERC with low power, (c) trERC with high power and (d) trESA+roERC. The horizontal arrow in (b) demonstrates the low SNR and contrast resulting from limited peak B_1^+ with the trERC when using a low power setting optimizing contrast in the peripheral zone. When a higher power setting was used to visualize the anterior side of the prostate, spins were over-flipped in the left peripheral zone as shown by the vertical arrow in (c). Note: the trERC image acquired at a low power setting was originally acquired with a smaller FOV.

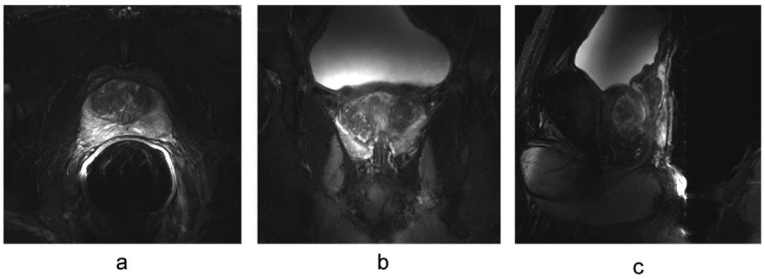

Figure 8.
High resolution anatomic T2w-TSE images were acquired in the (a) axial, (b) coronal and (c) sagittal planes with the trESA+roERC.

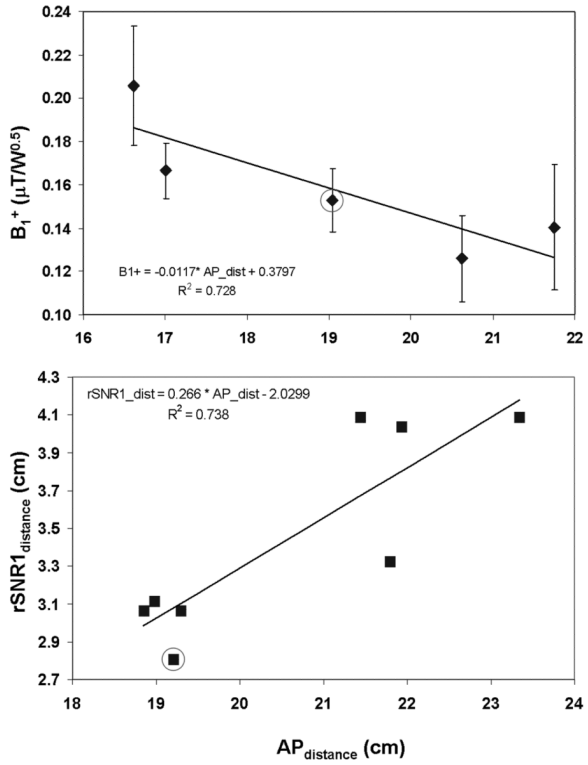

Figure 9.

Patient size dependent performance for the trESA on transmit (top) and receive (bottom). To evaluate transmit performance of the trESA, B_1^+ (mean and standard deviation) from a region around the prostate were measured for 5 subjects and plotted against their respective anterior-posterior width ($AP_{distance}$) (top). Receive performance (bottom) was evaluated by plotting the distance normal to the ERC where the ratio in SNR was equal between the internal and external coils ($rSNR1_{distance}$) against $AP_{distance}$. As expected, the performance of the external array decreased with increasing patient size on both transmit and receive. The B_1^+ and $rSNR1_{distance}$ values for the reference volunteer are indicated by the circled data points on each plot.

Table 1

Network analyzer evaluation of the coupling (S21) and quality factors both loaded (Q_L) and unloaded (Q_0), for the trESA, trERC and the roERC.[a]

	trESA	trERC	roERC
Coupling w/ trESA S21 (dB)	−26.4 ± 3.6 [b]	−36.2 ± 5.3 [c]	−48.0 ± 6.1 [c]
Loaded Q (Q_L)	39.1 ± 12.2	20.7 ± 4.5 [d]	17.7 ± 4.9 [d]
Unloaded Q (Q_0)	80.0 ± 13.8	196.3 ± 15.2 [d]	176.0 ± 5.3 [d]

[a] Results are reported as a mean ± standard deviation when measurements between multiple elements or multiple coils were made. All measurements acquired under loaded conditions were done so in vivo.

[b] S21 for the trESA were nearest neighbor measurements.

[c] S21 for the trERC and roERC were between the specific ERC coil and each of the trESA elements.

[d] Loaded and unloaded Q values of 3 coils of the given type (trERC or roERC) evaluated in vivo.

Table 2

Summary of transmit B_1 (B_1^+) statistics over the prostate, peak one gram averaged SAR normalized to 1 W per channel (SAR_{peak_norm}) and calculated time averaged power limits (TAP_{limit}).

		B1+				SAR [c]	TAP [d]
		Mean ± SD μT/W^{05}	Inhomo. [b] %	Min. μT/W^{05}	Max. μT/W^{05}	Peak_Norm W/kg	Limit W
trESA	In vivo [a]	0.152 ± 0.016	10	0.081	0.180	--	2.54
	Simulation	0.148 ± 0.023	15	0.084	0.177	6.29	--
trERC	In vivo [a,e]	1.24 ± 0.421	34	0.345	2.04	--	1.34
	Simulation	1.48 ± 0.972	66	0.305	7.35	6.64	--

[a] In vivo results are from the reference volunteer.

[b] Inhomogenetity is determined as the ratio of the standard deviation to mean.

[c] Peak one gram averaged SAR normalized to 1 W per channel. Therefore, these values are a result of 16 W total for the trESA and 1W total for the trERC.

[d] Time averaged power limits in Watts per channel.

[e] While the in vivo and simulated results are relatively consistent as shown by the profiles in Fig. 3 and 4, the DAM measurements do not faithfully measure the high B1+ close to the trERC coil. Therefore the simulated standard deviations and maximum B1+ values are more representative of expected in vivo values.

Table 3

Geometry factor (*g*-factor) table. Comparison of mean g-factors from simulation and in vivo measurement in the region of the prostate and from in vivo measurement for the artery for the trESA and trESA+roERC.

			Anterior-Posterior											
			Prostate						Artery					
			ERC			noERC			ERC			noERC		
		RF	1	2	3	1	2	3	1	2	3	1	2	3
In Vivio	Right-Left	1	1.00	1.02	1.23	1.00	1.08	1.30	1.00	1.01	1.04	1.00	1.01	1.05
		2	1.00	1.03	1.24	1.01	1.09	1.32	1.00	1.01	1.05	1.00	1.01	1.07
		3	1.02	1.06	1.44	1.06	1.16	1.52	1.03	1.04	1.08	1.02	1.04	1.10
		4	1.09	1.17	1.65	1.10	1.22	1.75	1.05	1.08	1.24	1.06	1.08	1.28
Simulation	Right-Left	1	1.00	1.01	1.13	1.00	1.01	1.24						
		2	1.01	1.02	1.16	1.01	1.03	1.28						
		3	1.06	1.08	1.32	1.06	1.09	1.42						
		4	1.16	1.20	1.63	1.14	1.20	1.77						